Implications of Multiple Corona Bursts in Lightning Processes for Radio Frequency Interferometer Observations

Liu, Ningyu; Scholten, Olaf; Dwyer, Joseph R.; Hare, Brian M.; Sterpka, Christopher F.; Tilles, Julia N.; Lind, Frank D.

Link to publication in University of Groningen/UMCG research database

Geophysical Research Letters®

Key Points:

- Complications of lightning radio interferometer data interpretation due to random nature of the emission sources are investigated
- Corona bursts observed by LOFAR may be seen as a fast ($>10^7$ m/s) moving source with power variation by short-baseline interferometers
- Requirements for radio interferometers to resolve corona bursts occurring in close spatial and temporal proximity are examined and discussed

Author Contributions:

Conceptualization: Ningyu Liu
Funding acquisition: Ningyu Liu
Investigation: Ningyu Liu, Olaf Scholten, Joseph R. Dwyer, Brian M. Hare, Christopher F. Sterpka
Methodology: Ningyu Liu, Olaf Scholten, Joseph R. Dwyer, Brian M. Hare, Julia N. Tilles, Frank D. Lind
Project Administration: Ningyu Liu
Software: Ningyu Liu
Visualization: Ningyu Liu
Writing – original draft: Ningyu Liu
Writing – review & editing: Ningyu Liu, Olaf Scholten, Joseph R. Dwyer, Brian M. Hare, Christopher F. Sterpka, Julia N. Tilles, Frank D. Lind

Implications of Multiple Corona Bursts in Lightning Processes for Radio Frequency Interferometer Observations

Ningyu Liu[1] , Olaf Scholten[2] , Joseph R. Dwyer[1] , Brian M. Hare[2] , Christopher F. Sterpka[1] , Julia N. Tilles[3] , and Frank D. Lind[4]

[1]Department of Physics and Astronomy & Space Science Center (EOS), University of New Hampshire, Durham, NH, USA, [2]Kapteyn Astronomical Institute, University Groningen, Groningen, The Netherlands, [3]Sandia National Laboratories, Albuquerque, NM, USA, [4]MIT Haystack Observatory, Westford, MA, USA

Abstract Recent observations from LOFAR indicate that multiple, spatially distributed corona bursts can occur in lightning processes with a timescale of 10 microseconds. The close proximity of the corona bursts in space and time poses a great observation challenge for short-baseline (typically ≤100 m) radio interferometers. This paper reports simulations to show the interferometry results that would be obtained with such an interferometer. In particular, spatially-separated corona bursts at fixed locations may be seen as a fast ($>10^7$ m/s) propagating source with large power variation if the resolution of the instrument is greater than the spatial separation of the bursts. The implications and suggestions for lightning interferometry studies are discussed in the paper.

Plain Language Summary Lightning evolution contains brief processes that are critical to its channel formation, but their physical mechanisms are poorly understood at present. Those processes emit very high frequency radio emissions, and radio sensor arrays have been used to detect those emissions to investigate their source processes. The latest observations from the large radio telescope LOFAR show that multiple, intense bursts of radio emission at discrete locations occur in those processes. Here we report simulations to show that such bursts are seen as a fast propagating wave for a short-baseline lightning radio sensor array. Our study suggests that caution is required when interpreting the observations made with such a radio sensor array.

1. Introduction

Lightning is a complex and multiscale electrical phenomenon that generates a broad spectrum of electromagnetic radiation. Fast electrical discharge processes occur during lightning development and they generate high frequency (HF, 3–30 MHz) and very high frequency (VHF, 30–300 MHz) electromagnetic emissions. These radio frequency (RF) emissions have been utilized to map and/or image lightning via some form of interferometry analysis. Important advances have recently been made based on broadband HF/VHF interferometer observations. These include identification of fast breakdown processes capable of initiating lightning (Huang et al., 2021; Rison et al., 2016; Stock et al., 2017; Tilles et al., 2019), measurement of perpendicular-to-channel polarization of the radiation of dart leaders (Shao et al., 2018), discovery of needle-like structures on positive leaders (Hare et al., 2019; Pu & Cummer, 2019), and observation of corona bursts of negative leaders at high altitudes (Scholten et al., 2021a). Because the lightning VHF sources can have complex temporal, spatial, and spectral properties, the radiation amplitude has a very large dynamic range, and they occur in a generally noisy environment, lightning interferometer observation and interpretation is definitely not a trivial task.

Modeling and theoretical work has shown that filamentary streamer discharges can radiate strongly in the HF and VHF bands (Shi et al., 2016, 2019), and they are believed to be the main source of the HF and VHF radiation from lightning (Liu & Dwyer, 2020; Liu et al., 2019, 2020). For many lightning processes, such as a leader step or lightning initiating fast breakdown, a large number (10^5–10^8) of streamers are believed to be involved (Liu & Dwyer, 2020; Liu et al., 2019, 2020). Those processes have a typical timescale of at least 1 microsecond and a spatial scale of at least a few meters, in contrast to the nanosecond timescale and centimeter spatial scale of a streamer. The large difference in those scales implies that there is inherent random nature in both spatial and temporal distributions of streamer occurrences in a lightning process.

In this study, we attempt to demonstrate how the random nature of streamer occurrences in a lightning process can complicate the analysis of lightning interferometer observations. Our study focuses on the initiation stage of

lightning, which typically contains only few channel branches, making the analysis of the interferometer observation easier. One common feature in the RF observation of lightning initiation is that a train of strong bipolar pulses occurs in the first few milliseconds (e.g., Belz et al., 2020; Marshall et al., 2014; Nag et al., 2009; Tilles, 2020). They are called initial breakdown pulses (IBPs), which are best observed by a RF sensor sensitive to lower RF frequency bands (e.g., 1 kHz-1 MHz). The duration of an IBP varies from 20 to 100 μs, with a mean of ∼60 μs. There are usually narrow subpulses superimposed on the initial half cycle of the waveform (e.g., Belz et al., 2020; Nag et al., 2009; Tilles, 2020).

Broadband, short-baseline (≤100 m) VHF interferometers for lightning observation typically consist of three radio sensors (Belz et al., 2020; Lyu et al., 2019; Rison et al., 2016; Shao et al., 2018; Stock et al., 2014, 2017; Sun et al., 2013; Tilles et al., 2019, 2020). The passband of the sensor spans from the upper HF band to the lower VHF band, for example, 10–90 MHz for the interferometer developed by the New Mexico Tech (Rison et al., 2016; Stock et al., 2014). The nominal angular resolution limit (i.e., the minimum angular separation of sources that can be resolved) for non super-resolution analysis is $\lambda/b \simeq 0.06$ radians, where λ is the wavelength and b is the baseline length, corresponding to 600 m at a distance of 10 km. The observations obtained with such an interferometer indicate that IBPs are coincident with strong VHF bursts and the VHF source activity shows greatly accelerated vertical motion over a distance of 100 m or so, typically during the initial half cycle of the IBP. The speed of the accelerated vertical motion exceeds 10^7 m/s (Belz et al., 2020; Krehbiel et al., 2021; Tilles, 2020). It has been proposed that IBPs are generated by fast breakdown, the same as narrow bipolar events (NBEs) (Belz et al., 2020; Krehbiel et al., 2021; Rison et al., 2016). These studies also found that gamma-ray production by lightning is directly connected to strong IBPs (Belz et al., 2020; Krehbiel et al., 2021). These authors have suggested that the narrow subpulses of IBPs are caused by spark-like transient conducting events (TCEs) embedded in fast breakdown, which likely occur in the leading edge of the developing streamer system (Attanasio et al., 2021; Krehbiel et al., 2021), and that TCEs trigger relativistic runaway electron avalanches to generate the gamma ray bursts.

High resolution observations of lightning have been obtained using the radio telescope LOFAR (Hare et al., 2019, 2020; Scholten et al., 2021a, 2021b). A recently-developed interferometry imaging code called interferometric 3-Dimensional (TRI-D) imager allows for determination of the emission source with meter scale accuracy at a time resolution of 100 ns, which is able to show the structures within a lightning leader step (Scholten et al., 2021b) (see (Hare et al., 2020) as well for the leader step structure). Detailed analysis of two IBP pulses observed by LOFAR using the TRI-D imager indicates that during an IBP multiple corona bursts occur at discrete locations within a volume of approximately 100^3 m^3 and there is no indication of a continuously propagating wave of intense electrical breakdown (Liu et al., 2022).

In this paper, we present simulations to show the results that short-baseline VHF interferometers with a small number of elements would obtain for IBPs consisting of multiple corona bursts and to give some ideas on the requirements to resolve those corona bursts.

2. Simulation Model

The main goal of simulation is to reproduce the interferometer images of synthetic VHF sources with specified spatial and temporal properties to understand the interferometer observations. The simulation consists of two main stages. The first stage simulates the VHF radiation from sources and the signals recorded by the sensors. At the second stage, the signals are processed and then used to obtain the image of the source with interferometry analysis. In this study, we explore how the results from interferometry analysis depend on the values of the several key parameters of the instrument for separating sources that occur in close space and time, including bandwidth, baseline, and integration time window.

Figure 1a shows a plan view of the observation geometry considered in our simulation. For simplicity, we consider an interferometer of three elements only. The sensors form an equilateral triangle as shown by the three closely-packed triangles in the figure, with one of the baselines parallel to the x axis. The VHF emission sources are at $x = y = 0$, and the plan distance from the center of the sensor triangle to the source is 8 km, that is, the center of the sensor triangle is at (8 km, −135°) in polar coordinates. The sources are at approximately 6 km altitude, and the distance from a sensor to the source is then about 10 km. This geometry closely represents the IBPs in cloud-to-ground lightning analyzed in (Tilles, 2020).
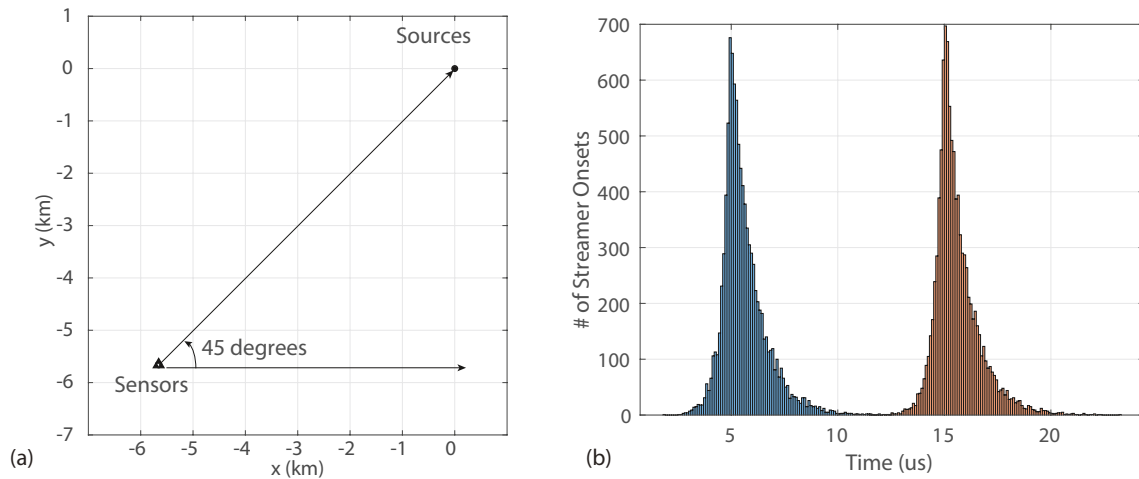
Figure 1. (a) Observation geometry in the simulation. (b) Histogram of the streamer onset.

In the simulation, the right most sensor is set as the reference sensor or viewing point, for which the interferometric images are constructed. Its location varies as the baseline changes, as the location of the sensor triangle center is fixed. The images are made for a small area of 1.6° azimuth and 2° elevation centered around the centroid of the sources. In this setting, the location of the center of the image relative to the reference antenna varies when the baseline length changes, and its azimuth is about 45°, but not exactly.

2.1. Simple Model for VHF Radiating Corona Bursts in IBPs

The VHF radiation source model used in our study is formulated based on LOFAR observations. As mentioned in the Introduction, the LOFAR data indicate that an IBP contains multiple corona bursts at different locations. In our simulation, we simply assume there are two corona bursts at two different altitudes: 6.1 and 6.0 km, that is, a 100 m height difference. We further assume that each burst contains 10^4 streamers, with the burst at the higher altitude occurring a few microseconds earlier. The onset times of the streamers within a burst are randomly drawn from an asymmetric Laplace distribution, with a 0.4 µs rise time and 1 µs fall time. Figure 1b shows the histogram of the streamer onset for a simulation case reported below, where the peaks of the two bursts are separated by 10 µs in time.

The streamers are assumed to be identical, and each generates a brief current pulse, which is assumed to be a double exponential function with a rise time of 1 ns and a fall time of 250 ns (Liu & Dwyer, 2020; Liu et al., 2019). The streamer current pulse and spectrum of the radiated field are shown in Figure S1 of Supporting Information S1.

2.2. Cross-Correlation Based Imaging Technique

To construct the image using the recorded signals, we adopt the same cross-correlation based imaging technique as Stock (2014) and Tilles et al. (2019). Cross-correlations between signals from pairs of sensors are calculated and used to assign intensities to image pixels. In addition, a beamforming technique is implemented in our simulation in order to improve the temporal resolution and accuracy. If we know where the source region is, we can use the center of the source region to estimate the respective time delays from the source to the sensors and then use the estimated delays to preliminarily align the signals. In this way, a smaller time window can be used to calculate the cross-correlation, which improves the temporal resolution of imaging (as all interferometric imaging requires integration over time). This idea has been explored by a recent study of Shao et al. (2020) and has been used in the LOFAR cross-correlation based impulsive imager (e.g., Scholten et al., 2021).

The above description can be represented mathematically as follows. Suppose the time series recorded by each sensor is denoted by $E_i(t)$ and the time-shifted signal by $E_i^o(t)$, we have

$$E_i^o(t) = E_i(t + \tau_i),\tag{1}$$

Table 1
Parameters of the Four Simulation Cases

Case	Burst time separation (μs)	Passband (MHz)	Baseline (m)	Integration time window (μs)	Frame time shift (μs)
A	10	10–90	100	1.4	0.35
B	10	30–80	100	0.1	0.1
C	5	30–80	800	0.1	0.1
D	10	100–200	200	0.02	0.02

where τ_i is the light travel time from the center of the source region to the ith sensor. The center of the source region is also set as the center (denoted by point o) of the image in the simulation. Let d_i^o represent the distance between that point and the ith sensor, then $\tau_i = d_i^o/c$.

To obtain the beamformed image frame corresponding to a time interval [t_n, $t_n + T$], where T is the time integration window size or exposure time of the image, the cross correlation between every pair of antennas i and j, R_{ij}^o, is calculated:

$$R_{ij}^o (t_n, \tau_{ij}) = \int_{t_n}^{t_n+T} E_j^o (t + \tau_{ij}) E_i^o(t)dt, \qquad (2)$$

where τ_{ij} is the time delay between the time-shifted series. Substituting Equation 1 into Equation 2 and changing the integration variable to $(t + \tau_i)$,

$$R_{ij}^o (t_n, \tau_{ij}) = \int_{t_n+\tau_i}^{t_n+\tau_i+T} E_j (t + \tau_{ij} + \tau_j - \tau_i) E_i(t)dt = R_{ij} (t_n + \tau_i, \tau_{ij} + \tau_j - \tau_i). \qquad (3)$$

Note $R_{ij}(t_n + \tau_i, \tau_{ij} + \tau_j - \tau_i)$ is the cross correlation between the non-shifted time series. From the observation geometry, we have $(d_{ij} \cos \alpha_{ij})/c = \tau_{ij} + \tau_j - \tau_i$, where d_{ij} is the baseline and α_{ij} is the directional angle. So

$$\tau_{ij} = \frac{d_{ij}\cos \alpha_{ij}}{c} - \tau_j + \tau_i. \qquad (4)$$

Equation 4 relates the directional angle to the delay between the shifted time series of the two sensors.

For each pixel, its directional angle with respect to a baseline is calculated first and the corresponding delay τ_{ij} between the two shifted time series is found by using Equation 4. The intensity of the pixel is then given by $R_{ij}^o (t_n, \tau_{ij})$. For the last step, interpolation is necessary as $R_{ij}^o (t_n, \tau_{ij})$ is found at discrete times only or only the cross correlations at discrete angles α_{ij} are known. Test runs indicate a higher order interpolation scheme is necessary to obtain accurate results, and cubic spline interpolation with the not-a-knot end condition is used in our study. Furthermore, the same interpolation scheme is also used to preliminarily align the signals at the beamforming step.

Intensities from all baselines are then added together to obtain the total intensity of that pixel. Denote the intensity of the nth frame from a baseline as $I_{ij} (n, \alpha_{ij}) = R_{ij}^o (t_n, \tau_{ij})$, we have

$$I \left(n, \vec{r} \right) = \sum_{i}^{M} \sum_{j=i+1}^{M} I_{ij} (n, \alpha_{ij}), \qquad (5)$$

where M is the total number of sensors.

If the ith antenna is the reference antenna, the time of the nth image frame is set to $(t_n + T/2 + \tau_i)$.

Finally, as demonstrated by Liu et al. (2021), this beamforming imaging method based on cross-correlation generates similar images as the interferometric technique based on delay and sum, which is implemented in the TRI-D imager of Scholten et al. (2021b).

3. Results

Results from four simulation cases are presented below, and Table 1 gives the parameters of each simulation case. We consider two values for the time separation between the two bursts: 5 and 10 μs. Given the duration of IBPs, 10 μs represents a moderate value of the time separation between the bursts, and 5 μs for relatively narrow IBP pulses. In calculating the radiated electric field, a time step of 1 nanosecond (i.e., 1 GHz sampling frequency) is used. For each case, a bandpass filter is applied to the recorded signals to obtain the specified bandwidth. Frame time shift is the time between two consecutive images, and there is no sample overlap between the images except for Case A, where the time shift is one quarter of the time integration window. Case A represents the typical
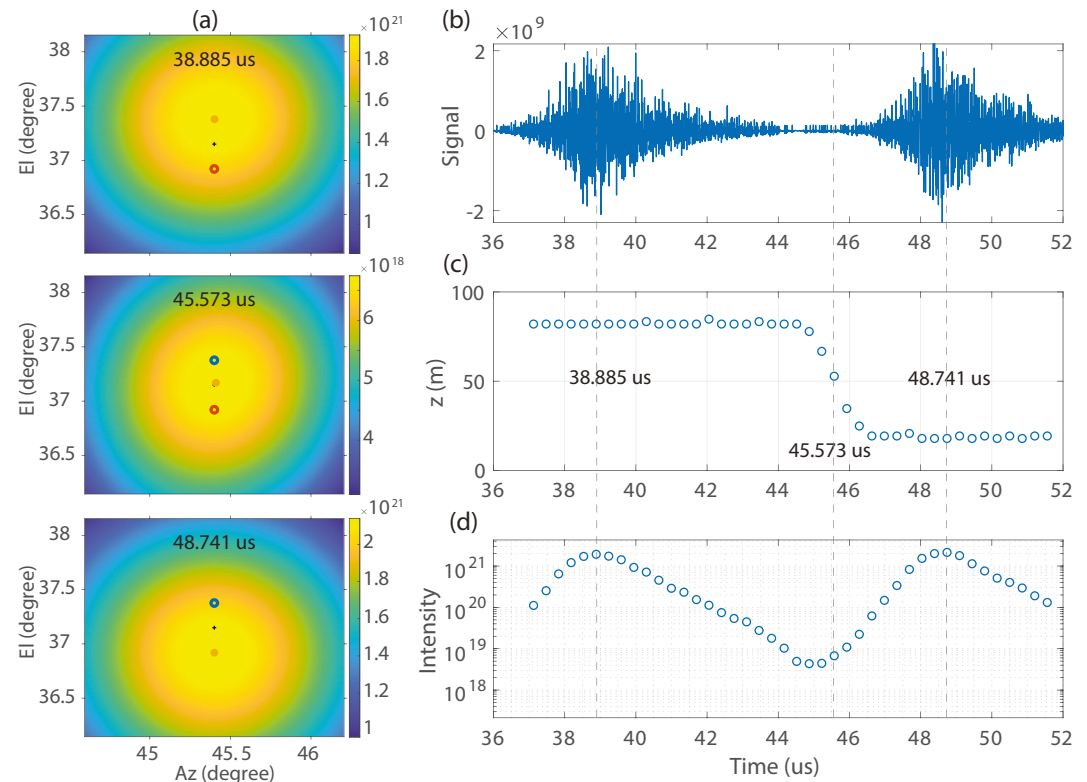
Figure 2. Case A simulation results. (a) Images at three different times. In each image, black '+' represents the center of the image, the blue and red circles denote the locations of the upper and lower streamer bursts, respectively, and the solid yellow circle shows the location of the maximum intensity pixel. The solid yellow circle masks an open circle when their locations are the same. (b) The bandwidth limited signal from the reference sensor. (c) The height of the maximum intensity pixel relative to 6 km altitude. (d) The value of the maximum intensity pixel.

configuration that was used in (Tilles, 2020; Tilles et al., 2019, 2020). As a large time integration window is used for this case, it is unnecessary to apply the beamforming technique. Except for the baseline and the number of antennas, Cases B and C represent the configuration of the latest LOFAR studies (Scholten et al., 2021b, 2022). The last case represents a moderate increase in the baseline of the interferometer used by Pu and Cummer (2019).

Figure 2 presents the simulation results from Case A. The three images correspond to three different time intervals, with their respective center times given in the figure. The bandwidth limited signal in Figure 2b shows although the two bursts are nominally separated by 10 μs, streamer activity is nearly continuous between them. The circles in Figure 2c give the heights (relative to 6 km) of the maximum intensity pixel of the images, while Figure 2d shows the temporal variation of the intensity of the same pixel. Each image in Figure 2a corresponds to either a peak or trough in Figure 2d. The large size of the main lobe in each image even under a narrow display intensity range is consistent with the nominal angular resolution of this case: $\lambda/b \simeq 0.06$ radians or 3.4°. Before 44 μs or slightly after 46 μs, the maximum intensity pixel overlaps with the location of the active streamer burst. The smooth transition in height from approximately 80–20 m, starting slightly after 44 μs and ending slightly after 46 μs, makes it appear that the source moves with a speed of $\simeq 3 \times 10^7$ m/s. The image at 45.753 μs shows that the maximum intensity pixel of that image is approximately at the mid point between the two bursts. Figure 2d shows that the intensity reaches the maximal value at the peaks of the bursts and is relatively small between the two bursts. The difference between the maximal and minimal values is, however, less than three orders of magnitude (note that the maximal intensity shown in the image at 45.753 μs is less than three orders of magnitude than the other two images), which is well within the dynamic range of a RF sensor of at least 12 bits. The image is made for a constant radial distance from the reference center, equal to the distance from the reference sensor to the center of the image at the mid point between the two bursts, that is, (0, 0, 6,050 m). This causes the heights of the two bursts are not exactly at 0 and 100 m (i.e., 6 and 6.1 km relative to ground), respectively.
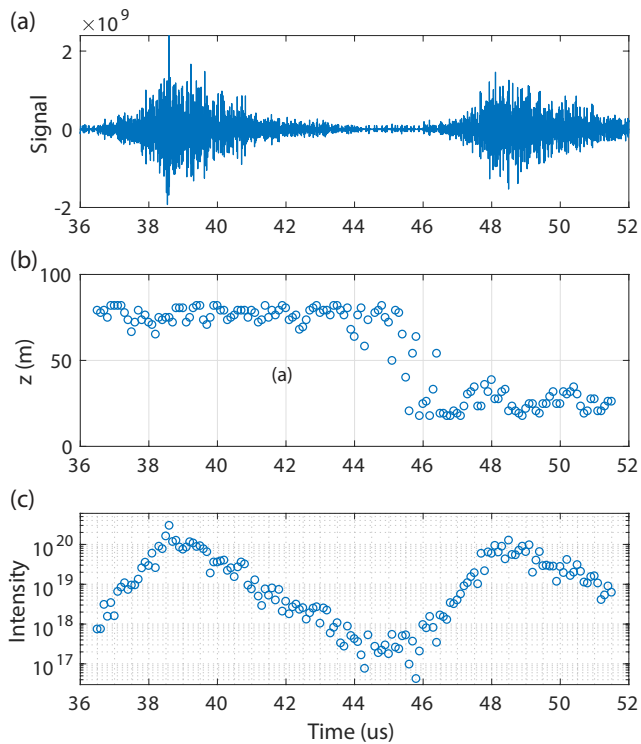
Figure 3. Case B simulation results. (a) The bandwidth limited signal from the reference sensor. (b) The height of the maximum intensity pixel relative to 6 km altitude. (c) The value of the maximum intensity pixel.

Figure 3 shows the simulation results from Case B. As the baseline is the same between this case and Case A and the frequency passband is approximately the same, the images of Case B are similar to those shown in Figure 2, which are omitted here. The apparent fast descending motion of the source can also be seen around 44–46 μs, with a similar change in the height and thus a similar speed. Because the time integration window is more than a factor of 10 smaller than Case A, the fluctuations in the height and intensity of the maximum intensity pixel are much larger. The smaller time integration window also results in smaller intensity values.
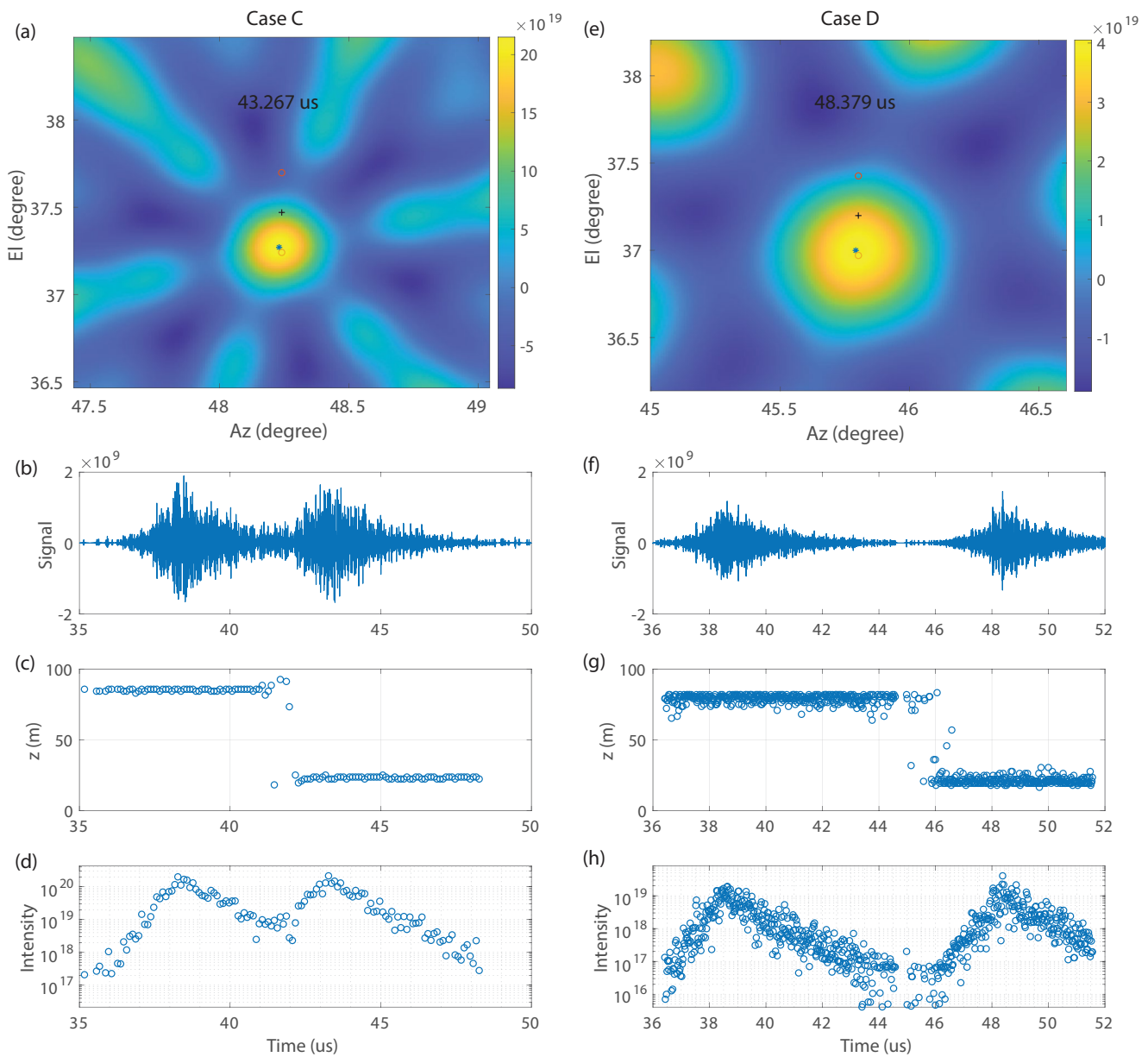
Figure 4 presents the results from cases C and D. For Case C, the baseline is increased to 800 m while the bandwidth is kept the same as Case B, resulting in a much better angular resolution. The main lobe in Figure 4a is much smaller in size, comparing to those in Figure 2a. Figure 4b shows that the streamer activity continuously occurs from the beginning of the first burst through the end of the second burst. It is clear, however, from Figure 4c that the sources have discrete locations instead of forming a gradual descending trajectory. Due to the random nature of the streamer onset in each burst, the location of the maximum intensity pixel during the time between the peaks of the two bursts may change suddenly, although bounded by the two true source locations. Finally, because of the smaller time separation between the bursts, the minimum intensity is less than two orders of magnitude smaller than the maximum intensity, as shown by Figure 4d. Overall, the increased baseline or improved angular resolution allows for resolving the two bursts even with a smaller time separation of 5 μs.

For Case D, both the passband frequency and baseline are moderately increased from Case A, so the angular resolution is better than Case A. The size of the main lobe shown in Figure 4e is smaller than that of Case A, but not as small as that of Case C. The time integration window 20 ns of this case is twice the reciprocal of the bandwidth, and beamforming is definitely required in order to use such a small time window. For this configuration, simply tracking the location of the maximum intensity pixel can tell that the radiation is not produced by a single moving source but by sources at discrete locations. Abrupt changes in the source height do occur in the time interval between the two bursts. The source height there is determined by which burst happens to generate stronger radiation in the corresponding 20 ns time window. Consistently, sudden changes occur in the intensity of the image.

4. Discussion

The present study investigates the artifacts in interferometer observations resulting from the complex properties of the lightning VHF emission source. Even for a simple case of two corona bursts with reasonable separation in space and time considered here, the simulation results show that entirely different views of the spatiotemporal evolution of the source can be obtained with different interferometer specifications and imaging parameters. It should be pointed out that in our simulation the bursts are at fixed locations and noise (e.g., RF emissions from other parts of lightning) is not included for convenience, which will make resolving the realistic corona bursts more challenging. A relevant question is if fast negative breakdown (FNB) in narrow bipolar events is caused by the apparent effect investigated here. Because FNB is the first initiating breakdown event and the recorded power does not show significant variation during its fast propagation stage, it is likely FNB is indeed a streamer-based ionization wave that propagates in the opposite direction of electric field.

To resolve the corona bursts that occur in close space and time, the spatial resolution of the instrument is the key. When the main lobe of the instrument is too large, extending over an area larger than the spatial separation between the bursts, the maximal intensity can appear at a location between them at the moment when the two bursts have comparable intensities. To improve the angular resolution λ/b, either the baseline, frequency, or both can be increased (assuming the uncertainties from the wave propagation are insignificant), as demonstrated by

Figure 4. Results from simulation cases C and D. (a and e) The image with the highest intensity during the entire simulation. In the image, black "+" represents the center of the image, the two circles give the locations of the two streamer bursts, and "∗" shows the location of the maximum intensity pixel. (b and f) The bandwidth limited signal from the reference sensor. (c and g) The height of the maximum intensity pixel relative to 6 km altitude. (d and h) The value of the maximum intensity pixel.

the simulation cases C and D. One factor that should also be taken into account is the source spectrum. The HF and VHF frequency spectrum of a corona burst is determined by the spectrum of individual streamers (Liu et al., 2019, 2020; Liu & Dwyer, 2020). Although the streamer spectrum considered here quickly rolls off above a few tens of MHz (see Figure S1 in Supporting Information S1), recent studies indicate the streamer spectrum in lightning processes can extend to higher frequency range (Pu et al., 2021, 2022). Therefore, increasing the frequency of the sensor should be effective in improving the resolution for at least some lightning processes.

It is also worth implementing algorithms or methods that can improve the temporal resolution of the imaging, such as the beamforming technique. Increasing the temporal resolution helps through reducing the chance of streamers from any two bursts to occur within the time window of an image. Its effectiveness depends on the number of streamers in a corona burst and separation between the bursts. In addition, future studies should explore imaging

techniques beyond time difference of arrival based approaches. Imaging algorithms utilizing larger numbers of baselines in Fourier based approaches combined with deconvolution such as CLEAN (Clark, 1980) are one direction similar to astronomical imaging. Multiple source direction of arrival algorithms based on covariance estimations such as MUSIC (Schmidt, 1986) are another direction. These algorithms have significant advantages for resolving ambiguities, using array degrees of freedom to enable estimation of multiple sources, and ultimately helping to resolve corona bursts. Additionally, these approaches are more suitable for the formal incorporation of array calibration to remove the effects of the interferometer element and array responses.

Finally, simulation can provide a good understanding of the dependence of the obtained source dynamics on the burst parameters to aid the analysis of the interferometer data. For instance, the apparent fast downward motion in Case A is inferred during the fall of the first burst and the rise of the second. The apparent speed then contains information about those times. In the case when radio sensors may be saturated during the corona bursts, and the interferometer does not have the resolution to resolve individual bursts, the apparent speed can still be determined (interferometry is generally robust in the case of signal saturation) and can still give information about the spatiotemporal evolution of the individual corona bursts. Another example is to understand and constrain the bidirectional development of fast breakdown reported by Huang et al. (2021). The bidirectional fast breakdown likely contains separate VHF sources that propagate either upward or downward. Simulations can provide the constraints on the source parameters in order for the sources to be resolved by a particular instrument. In fact, work is currently underway to simulate LOFAR observations to investigate accuracy and imaging artifacts of the LOFAR interferometry analysis (Scholten et al., 2022).

Data Availability Statement

The MATLAB scripts and functions used to obtain the results reported in the paper are available here: https://doi.org/10.5281/zenodo.5761824.

References

Attanasio, A., daSilva, C., & Krehbiel, P. (2021). Electrostatic conditions that produce fast breakdown in thunderstorms. *Journal of Geophysical Research: Atmospheres*, *126*(19), e34829. https://doi.org/10.1029/2021JD034829

Belz, J. W., Krehbiel, P. R., Remington, J., Stanley, M. A., Abbasi, R. U., LeVon, R., et al. (2020). Observations of the origin of downward terrestrial gamma-ray flashes. *Journal of Geophysical Research: Atmospheres*, *125*(23), e31940. https://doi.org/10.1029/2019JD031940

Clark, B. G. (1980). An efficient implementation of the algorithm 'CLEAN'. *Astronomy and Astrophysics*, *89*(3), 377.

Hare, B. M., Scholten, O., Dwyer, J., Ebert, U., Nijdam, S., Bonardi, A., et al. (2020). Radio emission reveals inner meter-scale structure of negative lightning leader steps. *Physical Review Letters*, *124*(10), 105101. https://doi.org/10.1103/PhysRevLett.124.105101

Hare, B. M., Scholten, O., Dwyer, J., Trinh, T. N. G., Buitink, S., ter Veen, S., et al. (2019). Needle-like structures discovered on positively charged lightning branches. *Nature*, *568*, 360–363. https://doi.org/10.1038/s41586-019-1086-6

Huang, A., Cummer, S. A., & Pu, Y. (2021). Lightning initiation from fast negative breakdown is led by positive polarity dominated streamers. *Geophysical Research Letters*, *48*(8), e91553. https://doi.org/10.1029/2020GL091553

Krehbiel, P., Remington, J., Stanley, M., Rison, W., Belz, J., & Fan, X. (2021). The nature and cause of initial breakdown pulses and the implications for streamer to leader and negative stepping processes. In *AGU fall meeting*. (Abstract AE25A-1917).

Liu, N. Y., Dwyer, J., Sterpka, C., Scholten, O., Hare, B. M., & Tilles, J. (2021). Understanding lightning interferometry images through simulation. In *AGU fall meeting*. (Abstract AE23A-02).

Liu, N. Y., & Dwyer, J. R. (2020). Thunderstorm high frequency radio bursts with weak low frequency radiation. *Geophysical Research Letters*, *47*(23), e90325. https://doi.org/10.1029/2020GL090325

Liu, N. Y., Dwyer, J. R., & Tilles, J. N. (2020). Electromagnetic radiation spectrum of a composite system. *Physical Review Letters*, *125*(2), 025101. https://doi.org/10.1103/PhysRevLett.125.025101

Liu, N. Y., Dwyer, J. R., Tilles, J. N., Stanley, M. A., Krehbiel, P. R., Rison, W., et al. (2019). Understanding the radio spectrum of narrow bipolar events. *Journal of Geophysical Research: Atmospheres*, *124*, 10134–10153. https://doi.org/10.1029/2019JD030439

Liu, N. Y., Scholten, O., Hare, B. M., Dwyer, J. R., Sterpka, C. F., Kolmašová, I., & Santolík, O. (2022). LOFAR observations of lightning initial breakdown pulses. *Geophysical Research Letters*, *49*(6), e2022GL098073. https://doi.org/10.1029/2022GL098073

Lyu, F., Cummer, S. A., Qin, Z., & Chen, M. (2019). Lightning initiation processes imaged with very high frequency broadband interferometry. *Journal of Geophysical Research: Atmospheres*, *124*, 2994–3004. https://doi.org/10.1029/2018JD029817

Marshall, T. C., Schulz, W., Karunarathna, N., Karunarathne, S., Stolzenburg, M., Vergeiner, C., & Warner, T. (2014). On the percentage of lightning flashes that begin with initial breakdown pulses. *Journal of Geophysical Research: Atmospheres*, *119*, 445–460. https://doi.org/10.1002/2013JD020854

Nag, A., DeCarlo, B. A., & Rakov, V. A. (2009). Analysis of microsecond- and submicrosecond-scale electric field pulses produced by cloud and ground lightning discharges. *Atmospheric Research*, *91*(2), 316–325. https://doi.org/10.1016/j.atmosres.2008.01.014

Pu, Y., & Cummer, S. A. (2019). Needles and lightning leader dynamics imaged with 100-200 MHz broadband VHF interferometry. *Geophysical Research Letters*, *46*(22), 13556–13563. https://doi.org/10.1029/2019GL085635

Pu, Y., Cummer, S. A., & Liu, N. (2021). VHF radio spectrum of a positive leader and implications for electric fields. *Geophysical Research Letters*, *48*(11), e2021GL093145. https://doi.org/10.1029/2021gl093145

Pu, Y., Liu, N., & Cummer, S. A. (2022). Quantification of electric fields in fast breakdown during lightning initiation from VHF-UHF power spectra. *Geophysical Research Letters*, *49*(5), e2021GL097374. https://doi.org/10.1029/2021GL097374

Rison, W., Krehbiel, P. R., Stock, M. G., Edens, H. E., Shao, X.-M., Thomas, R. J., et al. (2016). Observations of narrow bipolar events reveal how lightning is initiated in thunderstorms. *Nature Communications*, *7*(1), 1–12. https://doi.org/10.1038/ncomms10721

Schmidt, R. (1986). Multiple emitter location and signal parameter estimation. *IEEE Transactions on Antennas and Propagation*, *34*(3), 276–280. https://doi.org/10.1109/tap.1986.1143830

Scholten, O., Hare, B. M., Dwyer, J., Liu, N., Sterpka, C., Buitink, S., et al. (2021a). Distinguishing features of high altitude negative leaders as observed with LOFAR. *Atmospheric Research*, *260*, 105688. https://doi.org/10.1016/j.atmosres.2021.105688

Scholten, O., Hare, B. M., Dwyer, J., Liu, N., Sterpka, C., Buitink, S., et al. (2021b). Time resolved 3D interferometric imaging of a section of a negative leader with LOFAR. *Physical Review D*, *104*(6), 063022. https://doi.org/10.1103/PhysRevD.104.063022

Scholten, O., Hare, B. M., Dwyer, J., Liu, N., Sterpka, C., Kolmašová, I., et al. (2022). Interferometric imaging of intensely radiating negative leaders. *Physical Review D*, *105*, 062007. https://doi.org/10.1103/PhysRevD.105.062007

Scholten, O., Hare, B. M., Dwyer, J., Sterpka, C., Kolmašová, I., Santolík, O., et al. (2021). The initial stage of cloud lightning imaged in high resolution. *Journal of Geophysical Research: Atmospheres*, *126*(4), e33126. https://doi.org/10.1029/2020JD033126

Shao, X.-M., Ho, C., Bowers, G., Blaine, W., & Dingus, B. (2020). Lightning interferometry uncertainty, beam steering interferometry, and evidence of lightning being ignited by a cosmic ray shower. *Journal of Geophysical Research: Atmospheres*, *125*(19), e32273. https://doi.org/10.1029/2019JD032273

Shao, X.-M., Ho, C., Caffrey, M., Graham, P., Haynes, B., Bowers, G., et al. (2018). Broadband RF interferometric mapping and polarization (BIMAP) observations of lightning discharges: Revealing new physics insights into breakdown processes. *Journal of Geophysical Research: Atmospheres*, *123*(18), 10326–10340. https://doi.org/10.1029/2018JD029096

Shi, F., Liu, N. Y., Dwyer, J. R., & Ihaddadene, K. (2019). VHF and UHF electromagnetic radiation produced by streamers in lightning. *Geophysical Research Letters*, *46*, 443–451. https://doi.org/10.1029/2018GL080309

Shi, F., Liu, N. Y., & Rassoul, H. K. (2016). Properties of relatively long streamers initiated from an isolated hydrometeor. *Journal of Geophysical Research: Atmospheres*, *121*, 7284–7295. https://doi.org/10.1002/2015JD024580

Stock, M. (2014). *Broadband interferometry of lightning (Doctoral dissertation, New Mexico institute of mining and technology)*. Retrieved from https://www.proquest.com/dissertations-theses/broadband-interferometry-lightning/docview/1660201463/se-2

Stock, M. G., Akita, M., Krehbiel, P. R., Rison, W., Edens, H. E., Kawasaki, Z., & Stanley, M. A. (2014). Continuous broadband digital interferometry of lightning using a generalized cross-correlation algorithm. *Journal of Geophysical Research: Atmospheres*, *119*, 3134–3165. https://doi.org/10.1002/2013JD020217

Stock, M. G., Krehbiel, P. R., Lapierre, J., Wu, T., Stanley, M. A., & Edens, H. E. (2017). Fast positive breakdown in lightning. *Journal of Geophysical Research: Atmospheres*, *122*, 8135–8152. https://doi.org/10.1002/2016JD025909

Sun, Z., Qie, X., Liu, M., Cao, D., & Wang, D. (2013). Lightning VHF radiation location system based on short-baseline TDOA technique—Validation in rocket-triggered lightning. *Atmospheric Research*, *129*, 58–66. https://doi.org/10.1016/j.atmosres.2012.11.010

Tilles, J. N. (2020). *Broadband radio mapping and imaging of lightning processes*. Doctoral dissertation, University of New Hampshire. Retrieved from https://scholars.unh.edu/dissertation/2519

Tilles, J. N., Krehbiel, P. R., Stanley, M. A., Rison, W., Liu, N. Y., Lyu, F., et al. (2020). Radio interferometer observations of an energetic in-cloud pulse reveal large currents generated by relativistic discharges. *Journal of Geophysical Research: Atmospheres*, *125*(20), e32603. https://doi.org/10.1029/2020JD032603

Tilles, J. N., Liu, N. Y., Stanley, M. A., Krehbiel, P. R., Rison, W., Stock, M. G., et al. (2019). Fast negative breakdown in thunderstorms. *Nature Communications*, *10*(1), 1–12. https://doi.org/10.1038/s41467-019-09621-z